

Microbolometer Arrays for Airborne Fire Sensing

Mike Lampton, UCB SSL

April 18, 2014

1 Introduction

It is well known that wildfires can be detected and monitored from aircraft and spacecraft. Indeed the planned FUEGO geosynchronous-orbit mission (Pennypacker et al 2013; Lampton 2013) represents one contemporary approach for long term surveillance of fire-prone areas. To set the stage for airborne fire detection and measurement, in Figure 1 below I show the some contributors to the clear-sky vertical Earth spectral radiance.

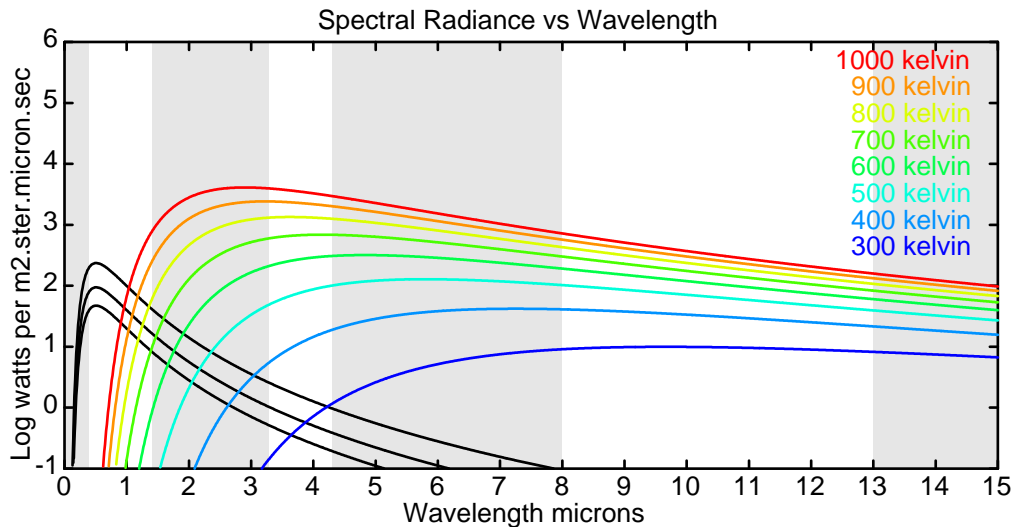


Figure 1: Earth radiance contributors from noon sunshine with albedos = 0.1, 0.2 and 0.5 (black curves); Earth heat, normally somewhat below a 300K blackbody (blue curve); and fire pixels whose equivalent temperatures range from 400K to 1000K (other colored curves). White zones are atmospheric transmission windows: from the left, VIS+NIR; MWIR; LWIR.

The principal atmospheric windows are the VIS+NIR ($0.4 - 1.4\mu m$) band, the MWIR ($3.3 - 4.3\mu m$) band, and the LWIR ($8 - 13\mu m$) band. The black curves show noon scattered solar radiances. The day and night thermal Earth radiance is complicated by surface materials, slopes, emissivities, but generally falls below the blue curve for $T=300K$ and emissivity=1. The higher colored curves show the higher equivalent temperature blackbody radiances.

2 Microbolometer Arrays

During these past twenty years, remarkable improvements in uncooled microbolometer array technology has improved their sensitivity, reliability, spatial resolution, and power requirement. Their chief market is thermal image sensing in the LWIR band, for which purpose they are usually fitted with bandpass filters to strongly reject light from the visible and MWIR bands to give the best possible thermometric accuracy, especially under daytime conditions. This application represents a huge market that a variety of developers and manufacturers are pursuing. In Figure 2 I have reproduced an electron micrograph from the LETI team (Becker et al 2012) of their microbolometer array structure, and show a highly simplified diagram of the steady-state heat flow. Far more detailed and dynamic analyses have been provided by Chen et al (2001), Bhan et al. 2009, etc etc.

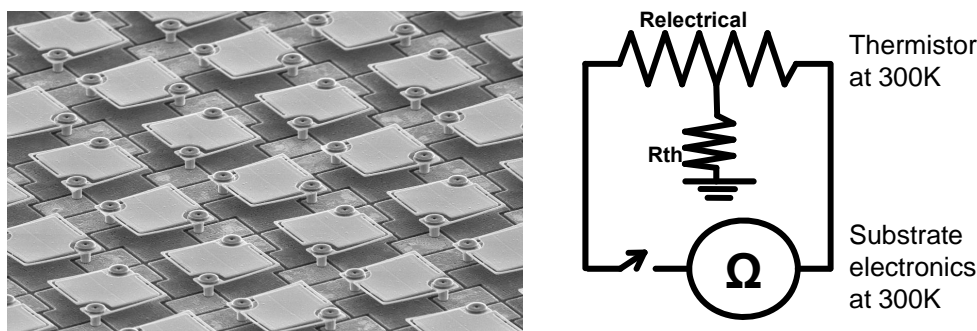


Figure 2: Left: a micrograph of a $12\mu m$ array of microbolometers on a VGA array, from the LETI group (Becker et al 2012 Fig 2). Each thermistor is elevated from the silicon substrate, with a thermal resistance of the order $100 - 200MK/W$. The substrate provides a matching grid of signal switches and ohmmeters (see Pochic et al 2009) allowing a large array to be read out in a raster pattern. Right: highly simplified diagram of ohmmeter, thermistor, and thermal resistor.

These LWIR arrays are exceptionally well suited for airborne detection and monitoring of wildfires. Lampton (2014) has recently proposed two practical airborne payloads that use a number of imaging VIS + LWIR camera-pairs, deployed in a pushbroom configuration, that deliver rapid coverage of large potential fire areas from robotic stratosphere UAVs.

Recently however several vendors have announced the availability of “broadband” microbolometer arrays. Microbolometers have inherent broadband performance, usually modified by reflector and absorber configurations to maximize their response in the LWIR band and minimizing response elsewhere. These newer broadband arrays have their reflectors and absorbers configured to deliver a more uniform spectral response. These modifications allow them to supplant or replace cooled image sensors in the MWIR ($3 - 5\mu m$) band. For airborne detection and monitoring of wildfire, the advantages of these new uncooled sensors are very significant: since no refrigeration is needed they offer much reduced electrical power consumption, reduced mass, lower cost, and improved ruggedness. Of course they are not as sensitive as cooled InSb or HgCdTe arrays, but they may offer enough sensitivity to assist with airborne fire detection. Here I compare MWIR vs. LWIR fire detection performance of broadband microbolometer image sensors.

In Figure 3 I have plotted a few sensor efficiency vs. wavelength curves that are representative of the work ongoing since about 2007. By “efficiency” I lump together the area filling factor and the bolometer absorption factor. These curves show that although the efficiency in the MWIR band may not be as high as in the traditional LWIR band, there is nonetheless an encouraging level of responsivity that (in view of the very high thermal output that wildfires deliver) could result in economical and practical sensors for airborne sensing in the MWIR region.

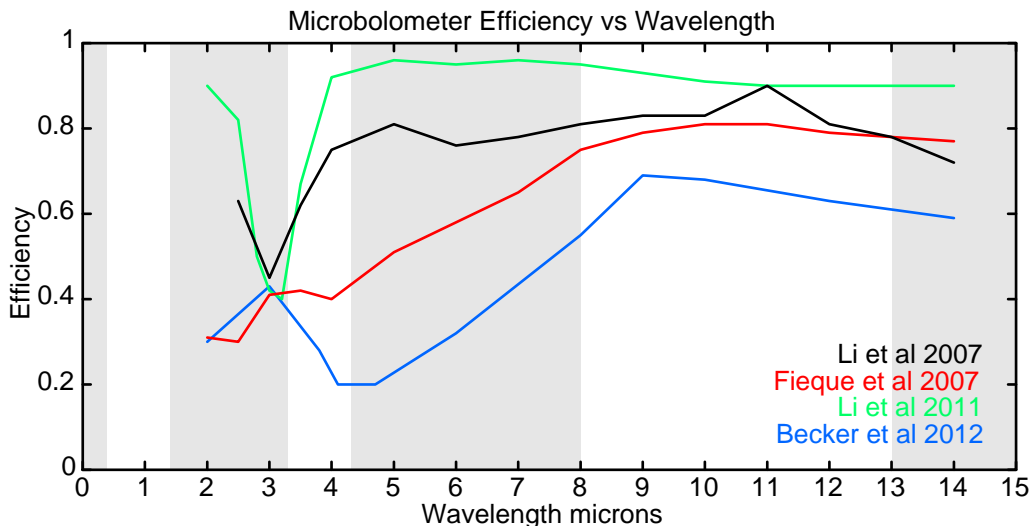


Figure 3: Thermal efficiencies E_{bolo} for four published microbolometer configurations, taken from the references cited. These efficiencies include both the area filling factor and the absorptivity.

3 Signal to Noise Ratio

For reliable detection and measurement accuracy, a key system parameter is the signal to noise ratio that a given scene, lens, filter, and sensor yields. Exhaustive studies of the sensor noise have been presented by Kohin and Butler (2004), by Niklaus et al (2008), and by Sizof (2012). Although there are a variety of noise contributors, nearly all of the video-rate 17 micron pitch arrays available today deliver a Noise Equivalent Delta Temperature $NEDT = 0.05K$ which is the RMS equivalent of the combined noise terms referred to the thermistor temperature. For the present purposes we shall adopt a model system based on such a nominal device, but using an appropriate filter and optical system to estimate its performance in the MWIR and (for comparison) the LWIR bands.

3.1 Signal

We take as the nominal signal a pixel area filled with a fire radiance whose dimensions on the Earth are a few meters, governed by the lens focal length and flight altitude. The power

incident on a pixel's area is

$$P_{pixel} = R_{scene} \cdot A_{lens} \cdot \Omega_{scene} \cdot \Delta\lambda \cdot E_{opt} \quad (1)$$

where R_{scene} is the scene spectral radiance, A_{lens} is the lens area, Ω_{scene} is the solid angle of the scene that one pixel intercepts, $\Delta\lambda$ is the bandwidth of the filter employed, and the overall system efficiency at the center of the band is the product of the combined filter and lens transmission E_{opt} . In other language, applying the brightness theorem to the optical train,

$$P_{pixel} = R_{scene} \cdot A_{pixel} \cdot \Omega_{lens} \cdot \Delta\lambda \cdot E_{opt} \quad (2)$$

where now the pixel area is A_{pixel} and the solid angle Ω_{lens} is the solid angle of the camera lens viewed by one pixel's area.

We describe the fire scene in terms of its effective temperature T which is the temperature of a perfectly emissive blackbody whose band radiance equals that of the fire at the pixel's location. In these terms, the Planck spectral radiance law applies, giving

$$R_{scene} = \frac{2hc^2}{\lambda^5 \cdot [\exp(hc/\lambda kT) - 1]} \quad (3)$$

3.2 Sampling

Before combining equations 2 and 3 we must address the related issues of image sampling, pixel pitch, and resolution. For complete freedom from aliasing, Fiete (1999) has shown that the sampling quality parameter $Q \equiv \lambda \cdot Fnum/Pitch = 2$ is required, and recommends that for practical image systems the rule $Q > 1$ be obeyed. (For a given focal length, a smaller Q value allows a faster optical train and higher sensitivity but increases image artifacts from aliasing.) The radius of the diffraction spot is $R_{spot} = \lambda \cdot Fnum$ so that $Q = R_{spot}/Pitch$. Here I adopt $Q = 1.2$ for both infrared bands, as a compromise between high sensitivity and tolerable image artifacts, and adopt the industry-standard pitch of $17 \mu m$. For both bands I adopt a common focal length of 100mm. In the LWIR band we obtain an optical speed of $f/2$ and a diffraction limited $R_{spot} = 20 \mu m$. In the MWIR, I also adopt a speed of $f/2$, and enlarge the spot size to the requisite $20 \mu m$ by defocussing. Adopting the most popular microbolometer array format, 640x480 pixels, the airborne system can then be scaled assuming a 20km stratospheric altitude as shown in Table 1 below.

MWIR and LWIR Cameras for Equal Fields, Equal Sampling

	MWIR	LWIR
Camera pixels across track	640	640
Camera pixels along track	480	480
Optical Throughput E_{opt}	0.7	0.7
Lens aperture, mm	50	50
Lens focal length, mm	100	100
Pixel size on ground, nadir, m	3.4	3.4
Spot radius, nadir, m	4.0 (defocus)	4.0 (diffraction)
Sampling $Q \equiv R_{spot}/Pitch$	1.2	1.2
One camera lateral field, nadir, km	2.18	2.18
Viewing time per pass at 150kts, sec	22	22
Pushbroom width, 10 cameras, km	24	24

A variety of camera quantities, formats, focal lengths, swath widths, etc could be explored, but the present purpose is to compare signal to noise ratios and the assumptions tabulated above will serve.

3.3 Noise

Because the fire signal (equation 2 above) is most conveniently expressed in steady-state power incident on a pixel area, I shall express the image noise level in those same terms, namely the Noise Equivalent Incident Power NEIP. In steady state, the NEIP is closely related to the bolometer's Noise Equivalent Absorbed Power NEAP and its own RMS temperature variation, the Noise Equivalent Delta Temperature NEDT:

$$NEIP = \frac{NEAP}{E_{bolo}} = \frac{NEDT}{E_{bolo} \cdot R_{thermal}} \quad (4)$$

Here, the efficiency factor E_{bolo} is the fraction of incident radiation that heats the bolometer, and $R_{thermal}$ is the effective thermal resistance of the device. To proceed with a noise estimate, I adopt NEDT=0.05K and $R_{thermal} = 100MK/W$ both of which have been quoted by various development teams. For the MWIR, I adopt $E_{bolo} = 0.5$ (but see Figure 3 above) and have NEIP=1 nW noise power level. For the LWIR, I adopt $E_{bolo} = 0.8$ and have NEIP=0.63 nW.

3.4 SNR

With these estimates, it is straightforward to estimate the signal to noise ratios appropriate for a single exposure frame, or for the coadded frames that are received during a single pass over the surveillance area. In this coaddition I assume that there are no systematic frame-to-frame pixel fluctuations that would interfere with the square-root improvement in SNR that independent measurements provide. This assumption is of course optimistic, and we might reasonably expect that the delivered coadded SNR lies somewhere between the single-frame and the single-pass estimates.

SNR for MWIR and LWIR Cameras

	MWIR	LWIR
E_{bolo}	0.5	0.8
Filled-pixel fire signal, nW	26	30
Noise equivalent incident power, nW	1	0.63
Signal to noise ratio, one exposure	26	48
Signal to noise ratio, one pass	666	1229

4 Conclusions

The foregoing material has set forth the case that uncooled MWIR microbolometer imagers can be usefully applied to the airborne fire detection task. Although they are far less sensitive than the established cooled InSb or HgCdTe photodiode array cameras, they nonetheless offer superior flightworthiness in terms of light weight, compactness, low power consumption, freedom from LN2 coolant or other refrigeration requirements, etc. Compared to the LWIR band, we might have expected the MWIR sensors to deliver equal or superior SNR owing to the higher MWIR fire radiance. They fail to do so because the MWIR bandwidth is less and because the bolometric efficiencies are somewhat poorer. Nonetheless the uncooled MWIR arrays appear to offer a useful additional airborne fire diagnostic, supplanting the thermal survey capability of a LWIR sensor group.

5 Future Work

Actual fires are not correctly described by a simple blackbody spectrum. Their spectra depend in a complicated way on every detail of the blaze: wind conditions, fuel identity, hillside slope, moisture content, and other factors. There is a wealth of fire data available, both hyperspectral and broadband, both from aircraft and spacecraft, that will be very useful in quantifying the relative benefits of three-band (VIS + MWIR + LWIR) fire surveillance vs two-band (VIS + LWIR). These data should be brought to bear on the airborne mission sensor complement cost-benefit trade.

There is a well-understood false-alarm zone at the subsolar azimuth due to daytime solar glint off small bodies of water. Other kinds of false alarms due to sunlight glints from terrestrial features also occur. If not identified on board, these false alarms could lead to a large number of hot-spot triggers. The broadband spectrum of solar + thermal is generally concave: high in the visible, low in the MWIR, and high in the LWIR (see Figure 1), whereas in contrast fire spectra are generally convex: low in the visible, high in the MWIR, and lower in the LWIR. Including the MWIR band could allow straightforward classification of hot spot features as to being concave (like false alarms) or convex (like fire signatures). Therefore triple-band surveillance could compare favorably to two-band surveillance in rejecting false alarms of many types.

The foregoing analysis studied only one highly favorable viewing condition (nadir; no clouds or haze; etc) but actual conditions complicate the surveillance task. A more comprehensive study should include these factors and estimate the detection yield and false alarm rate.

6 References

- Ajmera, S.K., et al, "Amorphous silicon thin-films for uncooled infrared microbolometer sensors," Proc SPIE 7660 (2010).
- Alicandro, C.J., and DeMarco, R.W., "1024x768 XGA uncooled camera core achieves new levels of performance in a small package," Proc SPIE 8012 (2011).
- Becker, S., et al., "Latest pixel size reduction of uncooled IR-FPA at CEA LETI," Proc SPIE 8541 (2012).
- Bhan, R.K., et al., "Uncooled infrared microbolometer arrays and their characterisation techniques," Defence Science Journal v.59 No.6 pp.580-589 (2009).
- Chen, C., et al., "Characterizations of VO₂-based uncooled microbolometer linear array," Sensors and Actuators A v.90 pp.212-214 (2001).
- Ciupa R. and Rogalski, A., "Performance limitations of photon and thermal infrared detectors," Opto-Electr. Rev. 5 No.4 pp.257-266 (1997).
- DRS Technologies, datasheet for DRS UC640-17 VO_x microbolometer camera, (2010).
- Durand, A., et al., "VGA 17um development for compact low power systems," Proc SPIE 8012 (2011).
- Fieque, B., et al., "Uncooled microbolometer detector: recent developments at ULIS," Infrared Phys. and Technol. 49 pp.187-191 (2007).
- Fiete, R. D., "Image quality and $\lambda FN/p$ for remote sensing systems, Opt. Eng. v.38 No.7 pp.1229-1240 (1999).
- Geoffray, H. and Guerin, F., "Measured performance of a low cost thermal infrared push-broom camera based on uncooled microbolometer FPA for space applications," Proc SPIE 4540 (2001).
- Holst, G. C., "Imaging system performance based on $F \lambda / d$," Opt. Eng. v. 46 No.10 (2007).
- Infrared Cameras Incorporated, datasheet ICI7640-P-series VO_x cameras (2011).
- Kohin, M., and Butler, N., "Performance limits of uncooled VO_x microbolometer focal plane arrays," Proc SPIE 5406 (2004).
- Kozlowski, L.J., and Kosonocky, W.F., "Infrared detector arrays," Chapter 33 of "Handbook

of Optics” Volume II, McGraw-Hill (2010).

Lampton, M., “FUEGO Mission Concept,” Proc. 1st Intl. FUEGO Workshop, UC/LBNL, Berkeley CA (Dec 2013).

Lampton, M., “FUEGO Airborne signal/noise study using LWIR microbolometer array cameras,” Proc. 2nd Intl. FUEGO Workshop, UC/LBNL, Berkeley CA (Apr 2014).

Li, C., Han C.J., and Skidmore, G. “Overview of DRS uncooled VOx infrared detector development,” Optical Engineering 50 No.6 (2011).

Li, C., et al., “Recent development of ultra small pixel uncooled focal plane arrays at DRS,” Proc SPIE 6542 (2007).

Li, C., et al., “Low cost uncooled VOx infrared camera development,” Proc SPIE 8704 (2013).

Li, C., et al., “Advancement in 17 micron pixel pitch uncooled focal plane arrays,” Proc SPIE 7298 (2009).

Lucke, R. L., and Kessel, R. A., “Signal to noise ratio, contrast to noise ratio, and exposure time for imaging systems with photon limited noise,” Opt. Eng. v.45 No 5 (2006).

Mather, J.C., “Bolometer noise: nonequilibrium theory,” Applied Optics v.21 pp.1125-1129 (1982).

Mottin, E., et al., “Uncooled amorphous silicon technology enhancement for 15 micron pixel pitch achievement,” Proc SPIE 4820 (2003).

Niklaus, F., et al., “Performance model for uncooled infrared bolometer arrays and performance predictions of bolometers operating at atmospheric pressure,” Infrared Phys. and Technology v.51 pp.168-177 (2008).

Pennypacker, C. R., et al., “FUEGO – Fire Urgency Estimator in Geosynchronous Orbit – a proposed early-warning fire detection system,” Remote Sens. v.5, pp.5173-5192 (2013).

Pochic, D., et al., “Uncooled amorphous silicon IRFPA for high performance and high volume applications,” Proc SPIE 7481 (2009).

Robert, P., et al., “Easy to use uncooled 1/4 VGA 17 micron FPA development for high performance compact and low power systems,” Proc SPIE 8353 (2012).

Rogalski, A., “Infrared detectors: status and trends,” Progress in Quantum Electronics v.27 pp.59-210 (2003).

Sizof, F., "IR region challenges: photon or thermal detectors? Outlook and means," Semiconductor Phys, Quant. Elec. and OptoElectronics v.15 No3 pp.183-199 (2012).

Sofradir datasheet, PV640 and Pico1024E FPAs, amorphous silicon technology Sofradir-EC Inc., (2012).

Talghader, J.J., et al., "Spectral selectivity in infrared thermal detection," Light Science and Applications v.1, pp.1-11 (2012).

Tezcan, D.S., et al., "A low cost uncooled infrared microbolometer focal plane array using the CMOS N-well layer," Proc 14th IEEE Intl MEMS conf "MEMS 2001" (2001).

Thurman, S. T., and Fienup, J. R., "Analysis of the general image quality equation," Proc SPIE v.6978 (2008).

Tissot, J-L., et al., "Status of uncooled infrared detector technology at ULIS France," Defence Science Journal v.63 No6 pp.545-549 (2013).

Tissot, J-L., et al., "High-performance uncooled amorphous silicon video graphics array and extended graphics array infrared focal plane arrays with 17 micron pixel pitch," Optical Eng., v.50 No.6 (2011).

Yon, J-J., Mottin E., and Tissot J-L., "Latest amorphous silicon microbolometer developments at LETI-LIR," Proc SPIE 6940 (2008).